



Research papers

Analytical model for predicting the longitudinal profiles of velocities in a channel with a model vegetation patch

Chao Liu^a, Yuqi Shan^{b,*}^a State Key Laboratory of Hydraulics and Mountain River Engineering, Sichuan University, Chengdu 610065, China^b College of Applied Mathematics, Chengdu University of Information Technology, Chengdu 610225, China

ARTICLE INFO

This manuscript was handled by Corrado Corradini, Editor-in-Chief, with the assistance of Gokmen Tayfur, Associate Editor

Keywords:

Velocity

Vegetation

Longitudinal profile

Predictive model

Flume experiments

ABSTRACT

This paper proposes an analytical model for predicting the longitudinal profile of depth-averaged streamwise velocities in a channel with an emergent array of rigid cylinders. The governing equation of the analytical model was derived from the momentum equation and flow continuity equation. The longitudinal transect through a flume with a vegetation patch was divided into four regions based on two length scales of flow adjustment upstream of and inside the array, and analytical solutions were proposed for the four regions. Laboratory experiments demonstrated that the array length does not influence flow adjustments near the upstream edge of the array, so the model can predict the longitudinal profile of streamwise velocity for either short or long arrays. Twenty groups of velocity data from different sources were used to verify the proposed model. The predicted velocities agreed well with the measured velocities, indicating that the model is capable of predicting the longitudinal profiles of the velocity upstream of and inside a model patch. The predicted velocity profile can be further employed to estimate regions of enhanced or diminished deposition of fine sediment or organic matter inside model patches.

1. Introduction

Vegetation is widely observed in natural rivers and plays an important role in river systems by altering flow structures, trapping sediment and changing bed morphology (e.g., Bennett et al., 2002; Gurnell et al., 2012; Schoelynck et al., 2012; Follett and Nepf, 2012; Kim et al., 2015; Liu et al., 2013, 2016; Shan et al., 2017, 2018; Hu et al., 2018; Gu et al., 2019; Yang et al., 2007). In the field, vegetation can be present in patches with finite length and width varying between 0.5 and 5 m (Sand-Jensen and Pedersen, 2008; Cornacchia et al., 2018). Understanding the interaction between flow and vegetation patches can help researchers further understand the local erosion and sediment deposition inside and around patches (Liu and Nepf, 2016; Tal and Paola, 2010). Specifically, inside a vegetation patch, the streamwise velocity within the interior adjustment region decreases as the distance from the upstream edge increases, and the velocity is constant beyond the region. When the velocity inside a patch decreases to a certain point, suspended sediment with organic material and nutrients deposits within the patch, thereby promoting the growth of new plants and increasing the density of plants (Vandenbruwaene et al., 2011; Gurnell et al., 2012). The deposition of suspended sediment inside patches depends on the strength of the stem-scale turbulence and the sediment

settling velocity, which can produce local sediment deposition (Sand-Jensen, 1998; Liu and Nepf, 2016). In addition, near the upstream edge of an emergent vegetation patch, the flow is deflected laterally out of the patch, leading to an increase in velocity and promoting bed erosion at side edges of the patch, which can prevent the lateral expansion of the vegetation patch (Sukhodolov and Sukhodolova, 2010; Bouma et al., 2007; van Wesenbeeck et al., 2008).

Many studies have used arrays of cylinders to simulate vegetation patches and have investigated the velocity evolution inside and outside model patches of emergent vegetation. Similar to field observations (introduced above), lateral flow deflection is observed near the upstream edge of the model patch, resulting in longitudinal velocity acceleration along two edges of the patch and longitudinal velocity deceleration inside the patch (e.g., Järvelä, 2005; White and Nepf, 2007; van Wesenbeeck et al., 2008; Zong and Nepf, 2011; Rominger and Nepf, 2011; Vandenbruwaene et al., 2011; Bouma et al., 2007; Huai et al., 2015). Therefore, in this study, model patches of emergent vegetation were constructed, and the velocities inside and upstream patches were measured. Meanwhile, we focus on developing a model for predicting the longitudinal profile of the time-averaged streamwise velocity upstream of and inside emergent model patches. The length scales of the velocity decay near the upstream edge of the model patch are

* Corresponding author.

E-mail address: yuqi.shan@qq.com (Y. Shan).<https://doi.org/10.1016/j.jhydrol.2019.06.076>

Received 17 April 2019; Received in revised form 25 June 2019; Accepted 27 June 2019

Available online 28 June 2019

0022-1694/ © 2019 Elsevier B.V. All rights reserved.

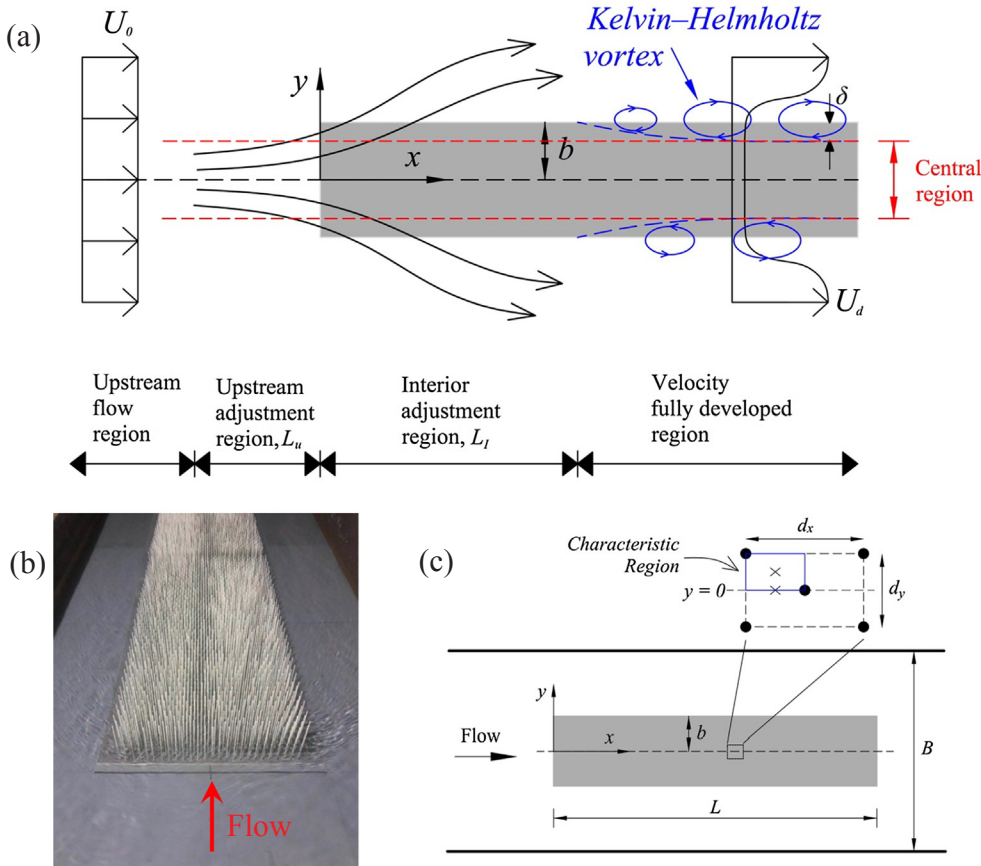


Fig. 1. (a) A sketch of flow adjustment along a cylinder array, based on the image in Rominger and Nepf (2011). The gray rectangle is the model vegetation patch, U_0 is the mean channel velocity, and b is the half patch width. At the two edges of the array, δ is the penetration distance that the Kelvin-Helmholtz (KH) vortex enters (blue arrow circles). The central region of the array ($-b + \delta \leq y \leq b - \delta$) is not affected by the KH vortices. L_u and L_i are the upstream and interior adjustment distances, respectively. (b) Image of the 5-m-long cylinder array in Case 3 ($C_d a b = 1.9$), in which the half patch width is $b = 80$ cm and the patch length is $L = 5$ m. (c) The arrangement of the model patch in our study. B ($= 2$ m) is the channel width; b and L are the half patch width and patch length, respectively. d_x is the longitudinal distance between in-row neighboring cylinders and d_y is the lateral distance between in-line neighboring cylinders. The blue box is a characteristic region, in which two velocities were measured; the measurement positions are denoted by “x”. The experimental parameters are summarized in Table 1. (For interpretation of the references to colour in this figure legend, the reader is referred to the web version of this article.)

introduced below. A sketch of flow adjustments associated with a model vegetation patch is shown in Fig. 1a. Inside the model patch, the distance over which the time-averaged streamwise velocity decreases to a minimum and remains constant is defined as the interior adjustment length, L_i . Rominger and Nepf (2011) found that the length scale L_i is dependent on both the vegetation drag and the patch width and proposed the following predictive equation for L_i :

$$L_i = (5.5 \pm 0.4) \sqrt{\left(\frac{2}{C_d a}\right)^2 + b^2} \quad (1)$$

where C_d is the drag coefficient, a ($= nd$) is the frontal area per patch volume, n is the cylinder density, d is the diameter of the cylinder, and b is the half patch width. Eq. (1) is valid over the range of $a = 0.05\text{--}0.8 \text{ cm}^{-1}$ and $b = 4\text{--}40$ cm (Rominger and Nepf, 2011).

Due to the lateral flow deflection, the mixing layer forms at the beginning of the patch edge ($x = 0$) and develops rapidly along the edge between $x = 0$ and L_i (Huai et al., 2015; White and Nepf, 2007). The absence of a Kelvin-Helmholtz (KH) vortex street between $x = 0$ and L_i has been numerically demonstrated (see Fig. 13 in Huai et al., 2015). Beyond the distance L_i , the mixing layer thickness stabilizes and becomes constant. If the shear between the outer and inner flow streams is strong enough to generate vortices, KH vortices form along the patch edge, and the vortices penetrate through the edge into the patch (White and Nepf, 2008; also see the cartoon in Fig. 1a). The momentum exchange driven by KH vortices at the edges of the patch leads to higher velocities in the penetration region than in the central region of the patch (White and Nepf, 2007, 2008). The penetration distance, δ , has been demonstrated to be highly correlated with the canopy density, $C_d a$, i.e., $\delta \sim (C_d a)^{-1}$ (Poggi et al., 2004; Nepf et al., 2007), and δ has different dependences for $C_d a < 1.5 \text{ cm}^{-1}$ and $C_d a \geq 1.5 \text{ cm}^{-1}$ (White and Nepf, 2008). Specifically, δ was correlated with the drag, $(C_d a)^{-1}$, for $C_d a < 1.5 \text{ cm}^{-1}$, whereas it was correlated

with the cylinder diameter, d , for $C_d a \geq 1.5 \text{ cm}^{-1}$ (see Fig. 10 in White and Nepf, 2008). Based on these correlations, White and Nepf (2008) proposed the following equation to predict δ :

$$\delta = \max [0.5(C_d a)^{-1}, 1.8d] \quad (2)$$

When the half patch width (b) is greater than the penetration distance (δ), the KH vortices cannot enter the patch central region. In this study, the central region inside the model patch ($-b + \delta \leq y \leq b - \delta$; see the region between the red dashed lines in Fig. 1a), in which the flow is not influenced by KH vortices, is our focus. An analytical model is proposed for predicting the longitudinal profile of the velocity in this region.

For vegetation patches with finite length and width (e.g., Chen et al., 2012; Liu and Nepf, 2016; Liu et al., 2018; Hu et al., 2018), a fully developed flow region is not created inside the patch because the patch length, L , is generally shorter than the interior adjustment region, L_i ($L < L_i$). Therefore, the velocity decreasing to a minimum and subsequent remaining constant value cannot be observed inside the patch, and KH vortices are not observed along the two patch edges. For submerged vegetation canopies, Chen et al. (2013) reported that the canopy length does not impact the vertical flow adjustment near the upstream edge of the canopy because streamwise velocities inside canopies with different lengths collapsed onto the same line in the longitudinal direction. However, the current study focuses on emergent patches, and the impact of patch length on the lateral flow adjustment near the upstream patch edge has not been examined yet. This effect is clarified in this study.

Some numerical models can simulate the flow through vegetation patches (e.g., Nicolle and Eames, 2011; Kim et al., 2018; Zhang et al., 2019). However, to our knowledge, there are no analytical models that can predict the longitudinal profile of velocities inside vegetation patches. In the field, detailed velocity measurements can be difficult to perform inside vegetation patches, particularly inside dense patches,

because the equipment is not easy to place. Based on this difficulty, a model capable of accurately predicting the velocity profiles inside patches would be very helpful. For laboratory experiments, a predictive model can save time and labor because researchers only need to measure a few velocities (e.g., the mean channel velocity and the velocity at the patch upstream edge). The present study proposes an analytical model for predicting the longitudinal profile of the streamwise velocity upstream of and inside the central region of emergent vegetation patches over a wide range of patch densities.

We first introduce our flume experiments in Section 2. Section 3 presents the experimental results, in which the length scales regarding flow adjustments are determined and the divided region method is introduced. The theory underlying the analytical model is then presented in Section 4. The published data for model validation are summarized in Section 5. Sections 6 and 7 present the model validation and application, respectively. Finally, a comparison with previous models and the limitations of the proposed model are discussed in Section 8.

2. Experimental methods

The experiments were performed in a 23-m-long and 2-m-wide flume with a 15-m-long test section and a horizontal bed. The flow discharge was measured using a triangle weir installed in front of the flume. The flow depth was measured using water level gauges along the flume. The mean channel velocity was measured using a Sontek acoustic Doppler velocimeter (ADV) 5 m upstream from the upstream edge of the model patch, where the velocity was not influenced by the patch. A discharge of $Q = 65 \pm 2$ L/s and a flow depth of $h = 17.8 \pm 0.2$ cm were used in all cases. The mean channel velocity was $U_0 = 18.0 \pm 0.5$ cm/s. The flow was turbulent in all cases with the channel Reynolds number $Re (= U_0 R/\nu) = 27,200$, with the hydraulic radius R and kinematic viscosity $\nu (= 0.01 \text{ cm}^2/\text{s})$. The flow was subcritical, with the Froude number $Fr (= U_0/\sqrt{gh}) = 0.14$, with gravitational acceleration g . Only one U_0 was considered in this study because the longitudinal profile of velocities was proven to be independent of U_0 under the turbulent flow ($Re \approx 5,000$ – $13,000$) and patch conditions $a = 0.04$ – 0.21 cm^{-1} and $b = 40$ cm (Zong and Nepf, 2011), and those conditions are similar to our experiments ($Re = 27,200$, $a = 0.048$ – 0.144 cm^{-1} and $b = 30$ – 40 cm). At the entrance of the flume, the water went through a flow straightener, producing a laterally uniform velocity profile. At the downstream edge of the flume, the tailgate was manually modified to achieve the target flow depth. The free surface slope was estimated using the measured water depths. The slope was $S \approx 1 \times 10^{-4}$, corresponding to variations in the water depth and the time-averaged streamwise velocity inside the model patch of 0.8% over the experimental section.

An array of rigid cylinders was constructed to simulate a vegetation patch (Fig. 1b). In the field, the patch length may be less than or greater than the interior adjustment length, L_I . To explore the influence of the patch length (L) on the velocity inside the patch, three patches with different lengths ($L = 1$ – 5 m) were designed depending on the flow blockage of the patch, $C_d ab$. For each flow blockage, two patches were designed shorter than L_I , and the third was longer than L_I . The patch width, $2b$ (b is the half patch width), varied between 60 and 80 cm. KH vortex streets occur in three cases (Cases 3, 6 and 9) with patches longer than L_I . The penetration distance, δ , was estimated using Eq. (2). In Cases 3, 6 and 9, δ ($= 3.5$ – 10.6 cm) was only 12–27% of the half patch width, $b = 30$ – 40 cm (see Table 1); thus, there was a central region inside the patch where KH vortices could not enter. Each model patch was constructed using plastic rigid cylinders. Cylinders were fitted into 1-cm-thick PVC boards with a staggered array of holes. The dowels were 20 cm long, so in this study all patches were emergent. Patches were placed 7 m downstream from the entrance of the test section at the center of the channel ($y = 0$ m). The bed friction coefficient of the PVC boards, C_f , was determined from the measured depth-averaged velocity,

U_d , and near-bed Reynolds shear stress, τ_{xz} ($= -\rho \bar{u'w'}$), in the preliminary experiment without cylinders, where u' and w' are fluctuating velocities in streamwise and vertical directions, respectively. U_d was calculated from vertical profiles of measured time-averaged streamwise velocities. τ_{xz} was measured at $z \approx 1$ cm above the PVC plate ($z/h \approx 0.06$, with $h = 17.8$ cm) and could be considered the same as the bed shear stress, $\tau_b (= \rho C_f U_d^2)$, according to Yang et al. (2015) (see Eq. (7) in their paper). In this study, $C_f = 0.006 \pm 0.001$ for the PVC boards, which was determined from $C_f = \tau_b/\rho U_d^2$.

The cylinders were rigid and exhibited no deformation during experiments. The cylinders do not represent a specific macrophyte but are realistic for reeds and cattails. The cylinder diameter, $d = 0.4$ cm, was chosen to fall within the range of stems and leaves of reeds, grasses and floodplain vegetation, $d = 0.1$ – 1 cm (Leonard and Luther, 1995; Lightbody and Nepf, 2006; Sand-Jensen, 1998). The cylinder density was $n = 0.12$ – 0.36 cm^{-2} , and the frontal area per patch volume was $a (= nd) = 0.048$ – 0.144 cm^{-1} . The solid volume fraction was $\phi (= \frac{\pi}{4} nd^2) = 0.015$ – 0.045 , which matched the observed range for cattails in natural rivers and wetlands, $\phi = 0.001$ – 0.04 (Grace et al., 1986; Coon et al., 2000). The drag coefficient, C_d , at the upstream edge of the cylinder array, which is close to that of an isolated cylinder for $Re_{d(0)} \geq 200$, is used to perform the prediction, where $Re_{d(0)} (= U_{d(0)} d/\nu)$ is the cylinder Reynolds number at the upstream edge ($x = 0$) of the array and $U_{d(0)}$ is the time-averaged streamwise velocity at $x = 0$. C_d is estimated using the equation of White (1991):

$$C_d = 1 + Re_{d(0)}^{-2/3} \quad (3)$$

In this study, $Re_{d(0)} \approx 600$, yielding $C_d \approx 1.1$. In natural rivers, the velocity approaching the canopy is $U_{d(0)} = 2$ – 40 cm/s (Sand-Jensen and Pedersen, 2008), and the stem diameter $d = 0.1$ – 1 cm (introduced above), yielding $Re_{d(0)} = 20$ – 4000 . Based on this, $C_d = 1$ – 1.14 , as estimated from Eq. (3). Therefore, in Cases 1–9, $C_d = 1.0 \pm 0.2$ was used with the possible variation for predicting velocities.

The longitudinal coordinate was x , with $x = 0$ representing the upstream edge of the patch; the lateral coordinate was y , with $y = 0$ representing the centerline of the channel and patch; and the vertical coordinate was z , with $z = 0$ representing the channel bed (Fig. 1). The streamwise velocity, $u(t)$, lateral velocity, $v(t)$, and vertical velocity, $w(t)$, were measured using a Sontek acoustic Doppler velocimeter (ADV) with a downward looking probe. The ADV was equipped on a measurement bridge, which could be moved in the x , y and z directions via a wireless software package. At each position, the recording period and frequency were 150 s and 50 Hz, respectively. The raw data were despiked using the method proposed by Goring and Nikora (2002). A MATLAB code was used to decompose velocities into time-averaged components (denoted u , v and w) and fluctuating components (denoted u' , v' , and w'). The noise in the streamwise velocity was less than 0.4 cm/s, which was determined by velocity measurements in still water. The vertical profiles of the time-averaged streamwise velocities were measured outside and inside the patch to obtain the depth-averaged streamwise velocity, $u_d (= \frac{1}{h} \int_0^h u \, dz)$. In both the bare channel and patch region, the streamwise velocity measured at the mid-depth ($z = 9$ cm) could be greater or smaller than u_d , and the difference between the mid-depth streamwise velocity and u_d was less than 6%. Therefore, the mid-depth velocity was considered to be the same as u_d . The velocity was measured at two positions at the mid-depth in a characteristic region between cylinders along the patch centerline (blue region in Fig. 1c), denoted “ \times ” ($y = 0$ and $dy/4$, where dy is the lateral distance between in-line neighboring cylinders). The longitudinal interval between two characteristic regions varied between 10 and 20 cm, depending on the patch density and length. U_d is the mean of the two measured velocities, which is representative of the velocity over half of the vegetation spacing, $dy/2$. The uncertainty in U_d indicates the variation in the velocity over the spacing. At all sampling positions at each longitudinal section ($y = 0$ or $dy/4$), the ADV was placed in the same

Table 1
Experimental parameters.^a

Case	<i>b</i> (cm)	<i>L</i> (cm)	<i>n</i> (cm ⁻²)	<i>a</i> (cm ⁻¹)	<i>C_dab</i>	φ	<i>L_u</i> (cm)	<i>L_l</i> (cm) ^b	<i>d_x</i> (cm)	<i>d_y</i> (cm)	δ (cm) ^c	λ	<i>U_{d(o)}</i> / <i>U_o</i>	RMSE ^d (cm/s)	RMSE/ <i>U_o</i> (%)
1	40	100	0.12	0.048	1.9	0.015	50 ± 25	–	4.6	3.6	–	14	0.79 ± 0.07	1.3	7.1
2	40	300	0.12	0.048	1.9	0.015	50 ± 25	–	4.6	3.6	–	14	0.94 ± 0.04	1.7	9.4
3	40	500	0.12	0.048	1.9	0.015	40 ± 20	350 ± 10	4.6	3.6	10.6	14	0.86 ± 0.04	1.3	7
4	30	100	0.18	0.072	2.2	0.023	20 ± 10	–	3.8	3	–	10	0.93 ± 0.04	2.5	13.7
5	30	250	0.18	0.072	2.2	0.023	40 ± 10	–	3.8	3	–	10	0.90 ± 0.03	2.4	13.1
6	30	400	0.18	0.072	2.2	0.023	30 ± 10	300 ± 20	3.8	3	6.9	10	0.85 ± 0.03	1.2	6.9
7	30	100	0.36	0.144	4.3	0.045	35 ± 15	–	2.6	2.2	–	10	0.77 ± 0.03	0.9	5.2
8	30	200	0.36	0.144	4.3	0.045	30 ± 15	–	2.6	2.2	–	10	0.84 ± 0.02	1.5	8.5
9	30	300	0.36	0.144	4.3	0.045	30 ± 15	210 ± 15	2.6	2.2	3.5	10	0.78 ± 0.02	1.2	6.5

^a *b* is the half patch width; *L* is the patch length; *n* is the cylinder density inside a model patch; *a* ($=nd$) is the frontal area per patch volume, in which *d* ($=0.4$ cm in this study) is the cylinder diameter; *C_d* is the drag coefficient at the upstream edge of a patch; *C_dab* is the flow blockage; φ ($=\frac{\pi}{4}nd^2$) is the solid volume fraction; *L_u* is the point at which the velocity started decreasing upstream of the patch; *L_l* is the point inside the patch at which the velocity achieved minimum or constant; *d_x* and *d_y* are the longitudinal and lateral distances between in-line and in-row neighboring cylinders; λ is the dimensionless parameter in the proposed analytical model; and *U_{d(o)}* is the measured velocity at the upstream edge of the patch (*x* = 0 cm). In all cases, the mean channel velocity, *U_o*, is 18.0 ± 0.5 cm/s, and the flow depth, *h*, is 17.8 ± 0.2 cm. The free surface slope, *S* ($\approx 1 \times 10^{-4}$), is the same in all cases.

^b The interior adjustment length, *L_i*, is estimated from measured velocities (see Section 4) and is given only for patches longer than *L_l*.

^c The penetration distance, δ , is estimated from Eq. (2).

^d RMSE is estimated from Eq. (4).

orientation and position relative to neighboring cylinders. Placing the ADV in a consistent orientation and at the same relative position can minimize the error induced by the spatial heterogeneity of the flow inside the cylinder array. At some longitudinal positions in Cases 3 and 9 ($\varphi = 0.015$ and 0.045 , respectively), the detailed lateral velocity profile in the characteristic region was recorded, in which the mean velocity of two positions was within 12% of the spatially averaged velocity. Similarly, the mid-depth velocity has been shown to be within 20% of the spatially averaged velocity for the cylinder arrays with $\varphi = 0.02$ – 0.1 (White and Nepf, 2007). The lateral profile of the velocity over the channel width was measured in the fully developed flow region ($> L_l$) inside the patch (e.g., *x* = 4.5 m inside the 5-m-long patch, in which *L_l* = 3.5 ± 0.1 m) to illustrate the flow symmetry on two sides of the patch.

The root mean square error (RMSE) is used to quantitatively compare the difference between the predicted and measured velocities and is expressed as:

$$RMSE = \sqrt{\frac{1}{N} \sum_{i=1}^N (U_{d(m)} - U_{d(p)})^2} \quad (4)$$

where *N* is the number of measurements and predictions and *U_{d(m)}* and *U_{d(p)}* are the measured and predicted velocities, respectively.

3. Experimental results

3.1. Flow adjustment length scales

The model patches longer than the interior adjustment length ($L > L_l$) were chosen to investigate two length scales (*L_u* and *L_l*) regarding the lateral flow adjustment upstream of and inside the patch. Taking Case 3 (*C_dab* = 1.9, *b* = 40 cm and *L* = 5 m) as an example, the longitudinal profile of the mean depth-averaged velocity, *U_d*, normalized by the mean channel velocity, *U_o*, is plotted against the distance, *x*, from the leading edge of the patch in Fig. 2. We first determine the adjustment region (*x* = $-L_u$ to 0 cm) upstream of the patch. The length of this region was defined as the distance over which 90% of the velocity change ΔU ($=U_o - U_{d(o)}$) occurred. That is, the upstream adjustment region begins at the point where $U_{d(x)} = U_{d(o)} + 0.9\Delta U$. In Fig. 2, *L_u* = 40 ± 20 cm, corresponding to $L_u/b = 1 \pm 0.5$. Second, inside the patch, the interior adjustment region was defined as the distance from the upstream edge of the patch to the point at which the velocity reaches a minimum and remains constant (*x* = 0 cm to *L_l*). In

Fig. 2, *L_l* = 350 ± 10 cm corresponds to $L_l/b = 8.8 \pm 0.3$. Similar steps were performed to obtain *L_u* for the patches shorter than *L_l* (Cases 1, 2, 4, 5, 7 and 8) and to obtain *L_u* and *L_l* for the patches longer than *L_l* (Cases 6 and 9). The two length scales are summarized in Table 1. In all cases, $L_u/b = 1.0 \pm 0.3$, indicating $L_u \approx b$. The measured L_l/b values ($=8.8 \pm 0.3$ in Case 3, 10.0 ± 0.7 in Case 6 and 7.0 ± 0.5 in Case 9) were close to the predicted L_l/b values ($=8.0$ in Case 3, 7.5 in Case 6 and 6.1 in Case 9) by the predictor of Rominger and Nepf (2011) (Eq. (1) in the Introduction). Hence, Rominger and Nepf's model was employed to predict *L_l* inside the patches for cases in which *L_l* was not reported.

3.2. Divided regions

Fig. 3 shows that in the central region of a model vegetation patch, the velocity mainly changed between *x* = $-L_u$ and *L_l*; thus, the longitudinal transect of a model patch can be divided into four regions (Regions 1–4 in Fig. 3). Region 1 is defined as the region of $x \leq -L_u$, over which *U_d* = *U_o*. Region 2 is defined as the distance ($-L_u \leq x \leq 0$) between the position at which *U_d* starts decreasing and the upstream edge of the patch (*x* = 0). Region 3 is defined as the distance ($0 \leq x \leq L_l$) from the upstream edge of the patch to the position at which *U_d* achieves a minimum and remains constant. Region 4 is defined at $L_l \leq x \leq L$, over which *U_d* is constant, indicating that the flow deep inside the patch is fully developed.

4. Theory

4.1. Equation derivation

For the flow in a channel with an emergent cylinder array, the equations for continuity and streamwise momentum are:

$$u \frac{\partial u}{\partial x} + v \frac{\partial u}{\partial y} + w \frac{\partial u}{\partial z} = \frac{1}{\rho} \left(\frac{\partial \tau_{xx}}{\partial x} + \frac{\partial \tau_{yx}}{\partial y} + \frac{\partial \tau_{zx}}{\partial z} \right) - F_x \quad (5)$$

$$\frac{\partial u}{\partial x} + \frac{\partial v}{\partial y} + \frac{\partial w}{\partial z} = 0 \quad (6)$$

where *u*, *v* and *w* are the time-averaged velocities in the *x*, *y* and *z* directions, respectively; ρ is the fluid density; τ is the Reynolds shear stress; and *F_x* is the drag force acting on the fluid in the streamwise direction.

This study proposes an analytical model for predicting the

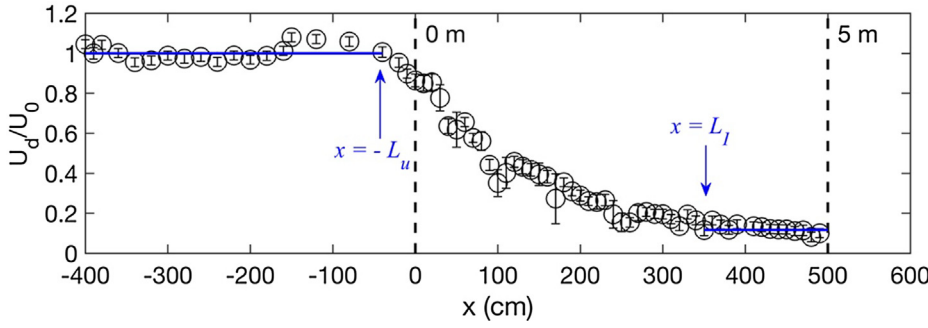


Fig. 2. Longitudinal profile of the mean depth-averaged streamwise velocity, U_d , normalized by the mean channel velocity, U_0 , in the central region of the 5-m-long cylinder array (Case 3, $C_{dab} = 1.9$). “0 m” and “5 m” indicate the upstream and downstream edges of the array, respectively. The upstream adjustment region is between $x = -L_u$ and 0 cm, and the interior adjustment region is between $x = 0$ cm and L_l . Based on the profile, $L_u = 40 \pm 20$ cm and $L_l = 350 \pm 10$ cm. This method also determines L_u and L_l for Cases 6 and 9 (Table 1).

longitudinal profile of depth-averaged streamwise velocity in the central region of model patches. The central region is $-b + \delta \leq y \leq b - \delta$, in which the velocity is not affected by the KH vortices along the two edges of the patch (Fig. 1a). Consequently, in the central region inside an array, the time-averaged velocity (u) and Reynolds shear stress ($\tau_{yx} = -\rho u'v'$) are constant in the lateral direction (Fig. 4). Similarly, Rominger and Nepf (2011) observed that u and $-\rho u'v'$ achieved constant values in the fully developed flow region in the central region of an emergent array (see Fig. 11 in their paper). Therefore, in the central region of a model patch, it is reasonable to assume the following equations over upstream and interior adjustment regions and the fully developed flow region:

$$\frac{\partial u}{\partial y} = 0 \text{ and } \frac{\partial \tau_{yx}}{\partial y} = 0 \quad (7)$$

The drag force F_x exerted on the water volume inside vegetation patches is defined as

$$F_x = \frac{1}{2} \frac{C_d a}{1 - \varphi} u^2 \quad (8)$$

The shear stress, τ_{xx} , in Eq. (5) is defined as

$$\tau_{xx} = -p + \Delta \tau_{xx} \quad (9)$$

where $p (= -\rho gh)$ is the fluid pressure, $\Delta \tau_{xx} (= 2\rho \varepsilon \frac{\partial u}{\partial x})$ is the additional shear stress and ε is the eddy viscosity. For a steady uniform flow, the free surface gradient, $\frac{\partial h}{\partial x} (= S)$, is equal to the bed slope, S_0 .

Combining Eqs. (5)–(9), we obtain the equation below:

$$\frac{\partial u^2}{\partial x} + \frac{\partial uw}{\partial z} = gS + \frac{1}{\rho} \frac{\partial}{\partial x} (\Delta \tau_{xx}) + \frac{1}{\rho} \frac{\partial \tau_{zx}}{\partial z} - \frac{1}{2} \frac{C_d a u^2}{1 - \varphi} \quad (10)$$

This model is proposed for an emergent vegetation patch so that the flow inside and outside the patch is two-dimensional. That is, the flow deflection mainly occurs in the longitudinal and lateral directions (x and y , respectively). The vertical velocity, w , is sufficiently small (≈ 0 cm/s, data not shown) at the surface of the channel bed ($z = 0$ cm) and water surface ($z = h$); thus, $\int_0^h \frac{\partial uw}{\partial z} dz = 0$ cm²/s². The shear stress, $\tau_{zx} (= -\rho u'w')$, is approximately zero at the water surface ($z = h$)

but is equal to the bed shear stress, $\tau_b (= \rho u_*^2)$, at the surface of the channel bed ($z = 0$ cm), where $u_* (= \sqrt{C_f U_d})$ is the shear velocity. The depth-averaged additional shear stress, $\Delta \tau_{xx(d)}$, is expressed as $\Delta \tau_{xx(d)} = 2\rho \varepsilon_d \frac{\partial U_d}{\partial x}$, in which ε_d (cm²/s) is the depth-averaged eddy viscosity proportional to the product of a length scale and a velocity scale. It is reasonable to assume that $\varepsilon_d = \lambda h u_* = \lambda h \sqrt{C_f} U_d$ with a non-dimensional parameter λ . We first discuss the order of the λ value. ε_d is of the order O(10) (cm²/s) for the local velocity $u \approx 10$ –60 cm/s, flow depth $h \approx 10$ –30 cm and the vegetation condition $\varphi \approx 0.07$ –0.2 (Lopez and Garcia, 1997; Vionnet et al., 2004; Choi and Kang, 2004). Therefore, λ is of the order O(1–10), estimated from h , C_f and U_d in this study. For a vegetated case, ε_d , h and C_f generally remain constant, so $\lambda (= \frac{\varepsilon_d}{h \sqrt{C_f} U_d})$ is inversely related to U_d . We then focus on the determination of λ . It is reasonable to use the measured $U_{d(0)}$ at the interface of Regions 2 and 3 (the upstream edge of the patch, $x = 0$ cm) to determine the λ value because it occurs only in the governing equation (Eq. (10)) for Regions 2 and 3. In our study, for each density, the mean of $U_{d(0)}/U_0$ for three patches was used to determine λ , so λ was the same for the three patches with the same density but different lengths (Table 1). Across all cases, the values of λ are summarized in Tables 1 and 2. When $U_{d(0)}$ cannot be measured, $U_{d(0)}$ can be estimated from the flow blockage C_{dab} and mean channel velocity U_0 (see the detailed discussion in Section 6).

Integrating Eq. (10) over the flow depth h , the governing equation is:

$$ghS + \lambda h^2 \sqrt{C_f} \frac{\partial^2 U_d^2}{\partial x^2} - h \frac{\partial U_d^2}{\partial x} - \left(C_f + \frac{1}{2} \frac{C_d a h}{1 - \varphi} \right) U_d^2 = 0 \quad (11)$$

in which $U_d h = \int_0^h u dz$. As introduced in Section 3.2, U_d varies at $-L_u \leq x \leq L_l$ (Regions 2 and 3, see Fig. 3), resulting in $\frac{\partial U_d^2}{\partial x} \neq 0$. Therefore, Eq. (11) is valid in Regions 2 and 3. However, U_d is constant at $x \leq -L_u$ in Region 1 and at $L \geq x \geq L_l$ in Region 4 (Fig. 3), yielding $\frac{\partial U_d^2}{\partial x} = 0$ and $\frac{\partial^2 U_d^2}{\partial x^2} = 0$. Eq. (11) is simplified as

$$ghS - \left(C_f + \frac{1}{2} \frac{C_d a h}{1 - \varphi} \right) U_d^2 = 0 \quad (12)$$

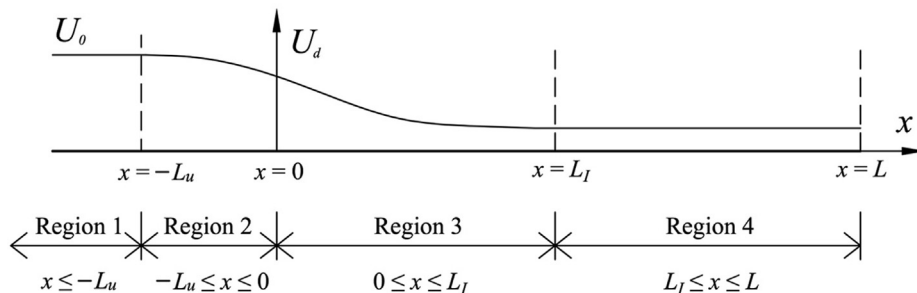


Fig. 3. Method of dividing regions in the central region of the model vegetation patch. Four regions are divided based on two length scales (L_u and L_l). $x = 0$ indicates the upstream edge of the patch.

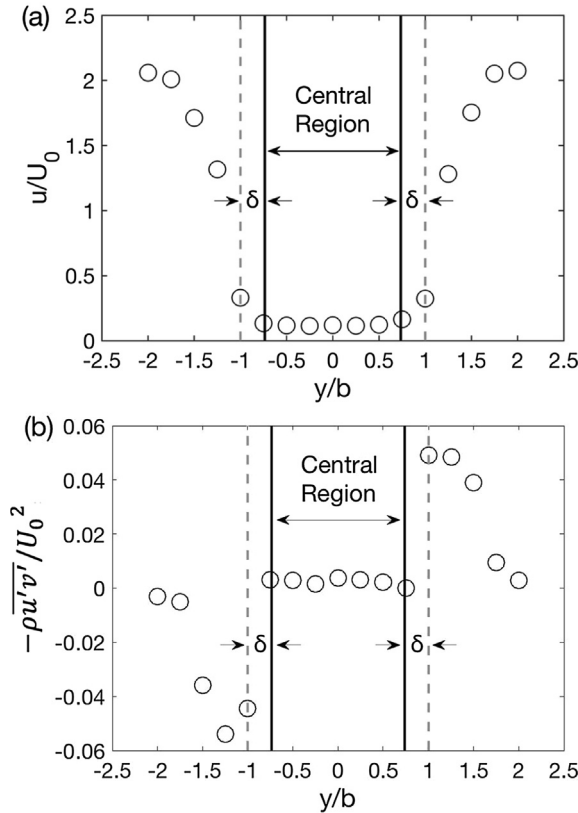


Fig. 4. Lateral profiles of velocity statistics in the fully developed region inside the array at $x = 450 \text{ cm} > L_f (= 350 \pm 10 \text{ cm})$, based on the data from Case 3 with $C_d a b = 1.9$. The half patch width is $b = 40 \text{ cm}$. Each point indicates the mean of two measurements at the middle depth ($z = 9 \text{ cm}$). (a) Time-averaged streamwise velocity, u , normalized by the mean channel velocity U_0 ; (b) Reynolds shear, $-\rho u'v'$, normalized by U_0^2 . The two vertical dashed lines indicate the two edges of the array. The region between the two vertical solid lines indicates the central region of the array. The uncertainty in u/U_0 and $-\rho u'v'/U_0^2$ is comparable to or smaller than the symbol size. The penetration distance, δ , is estimated from Eq. (2).

The analytical solutions, Eqs. (13)–(16), in the four regions were solved from Eqs. (11) and (12). Specifically, in Region 1, the analytical solution, Eq. (13), was obtained from Eq. (12) with $a (=nd) = 0 \text{ cm}^{-1}$ due to $n = 0 \text{ cm}^{-2}$.

$$U_d = \left(\frac{ghS}{C_f} \right)^{1/2} \quad (13)$$

In Region 2, the analytical solution, Eq. (14), was solved from Eq. (11) with $a (=nd) = 0 \text{ cm}^{-1}$ as follows:

$$U_d = (A_1 e^{r_1 x} + A_2 e^{r_2 x} + \omega_1)^{1/2} \quad (14)$$

in which A_1 and A_2 are unknown constants, $r_1 = \frac{h + \sqrt{h^2 + 4\lambda h^2 \sqrt{C_f}(C_f)}}{2\lambda h^2 \sqrt{C_f}}$,

$$r_2 = 2h - r_1 \text{ and } \omega_1 = \frac{ghS}{C_f}.$$

In Region 3, the analytical solution, Eq. (15), was solved from Eq. (11) as follows:

$$U_d = (A_3 e^{r_3 x} + A_4 e^{r_4 x} + \omega_2)^{1/2} \quad (15)$$

in which A_3 and A_4 are unknown constants,

$$r_3 = \frac{h + \sqrt{h^2 + 4\lambda h^2 \sqrt{C_f}(C_f + \frac{1}{2} \frac{C_d a h}{1-\phi})}}{2\lambda h^2 \sqrt{C_f}}, r_4 = 2h - r_3 \text{ and } \omega_2 = \frac{ghS}{C_f + \frac{1}{2} \frac{C_d a h}{1-\phi}}.$$

In Region 4, the analytical solution, Eq. (16), was obtained from Eq. (12) as follows:

$$U_d = \left(\frac{ghS}{C_f + \frac{1}{2} \frac{C_d a h}{1-\phi}} \right)^{1/2} \quad (16)$$

In Eq. (16), ghS is generally constant in a case, so the depth-averaged velocity is determined by the bed drag, C_f , and vegetation drag, $\frac{1}{2} \frac{C_d a h}{1-\phi}$, with $a = nd$. If the vegetation drag is greater than the bed drag (i.e., $\frac{1}{2} \frac{C_d a h}{1-\phi} > C_f$), the vegetation drag dominates the drag resistance inside the patch, corresponding to a density n greater than the threshold $n_c (= \frac{C_f}{C_d} \frac{2(1-\phi)}{dh})$. In all cases (in this study and the published works introduced in Section 5), the vegetation drag dominates the velocity inside patches because $n (= 0.07\text{--}1.3 \text{ cm}^{-2}) \gg n_c (= 0.001\text{--}0.002 \text{ cm}^{-2})$.

4.2. Boundary conditions

The unknown parameters A_1 to A_4 in Eqs. (14) and (15) can be obtained by appropriate boundary conditions. At the interface of Regions 1 and 2 ($x = -L_u$), the depth-averaged streamwise velocity, U_d , calculated from Eqs. (13) and (14) must be the same. Thus, $U_{d(1)} = U_{d(2)}$ at $x = -L_u$ is the first boundary condition, in which the subscript “(i)” indicates the number of the region. At the interface of Regions 2 and 3 ($x = 0$), the continuities of U_d and of the longitudinal gradient of U_d must be considered, and these continuities are the second and third boundary conditions. At the interface of Regions 3 and 4 ($x = L_f$), U_d estimated from Eqs. (15) and (16) must be the same; thus, $U_{d(3)} = U_{d(4)}$ at $x = L_f$ is the fourth boundary condition. Overall, the four boundary conditions, which are shown below, can be used to solve for A_1 – A_4 :

Table 2

A summary of the experimental parameters in four published studies.^a

Source	Case	U_0 (cm/s)	b (cm)	a (cm^{-1})	$C_d a b$	ϕ	h (cm)	S (%)	L_f (cm)	δ (cm) ^b	λ	$U_{d(0)}/U_0$	RMSE (cm/s)	RMSE/ U_0 (%)
Rominger and Nepf (2011)	RN1	10	15	0.2	3	0.09	14	0.044	99	2.5	12	0.75	0.6	6.1
	RN2	10	6	0.8	4.8	0.38	14	0.044	36	1.1	8	0.58	0.9	9.2
	RN3	10	10	0.8	8	0.38	14	0.044	57	1.1	15	0.53	0.6	5.7
Zong and Nepf (2011)	ZN1	5	40	0.04	1.6	0.02	12	0.013	352	12.5	48	0.8	0.3	5.2
	ZN2	5	40	0.21	8.4	0.1	12	0.013	226	2.4	60	0.58	0.3	5.6
	ZN3	9	40	0.04	1.6	0.02	13	0.038	352	12.5	26	0.85	0.2	2.7
	ZN4	9	40	0.21	8.4	0.1	13	0.038	226	2.4	39	0.62	0.5	5.3
	ZN5	11.6	40	0.04	1.6	0.02	14	0.059	352	12.5	27	0.84	0.4	3.7
	ZN6	11.6	40	0.21	8.4	0.1	14	0.059	226	2.4	40	0.61	0.5	4.7
Chen et al. (2012)	–	9.8	21	0.06	1.3	0.03	13.3	0.042	214	8.1	19	0.84	0.7	6.8
Liu and Nepf (2016)	–	9.1	5	0.51	2.6	0.15	14	0.03	35	1	7	0.71	0.4	4

^a The notations have the same definitions as those in Table 1. L_f is estimated from Eq. (1); $U_{d(0)}/U_0$ is obtained from the measured velocities from the published literature.

^b The penetration distance, δ , is estimated from Eq. (2).

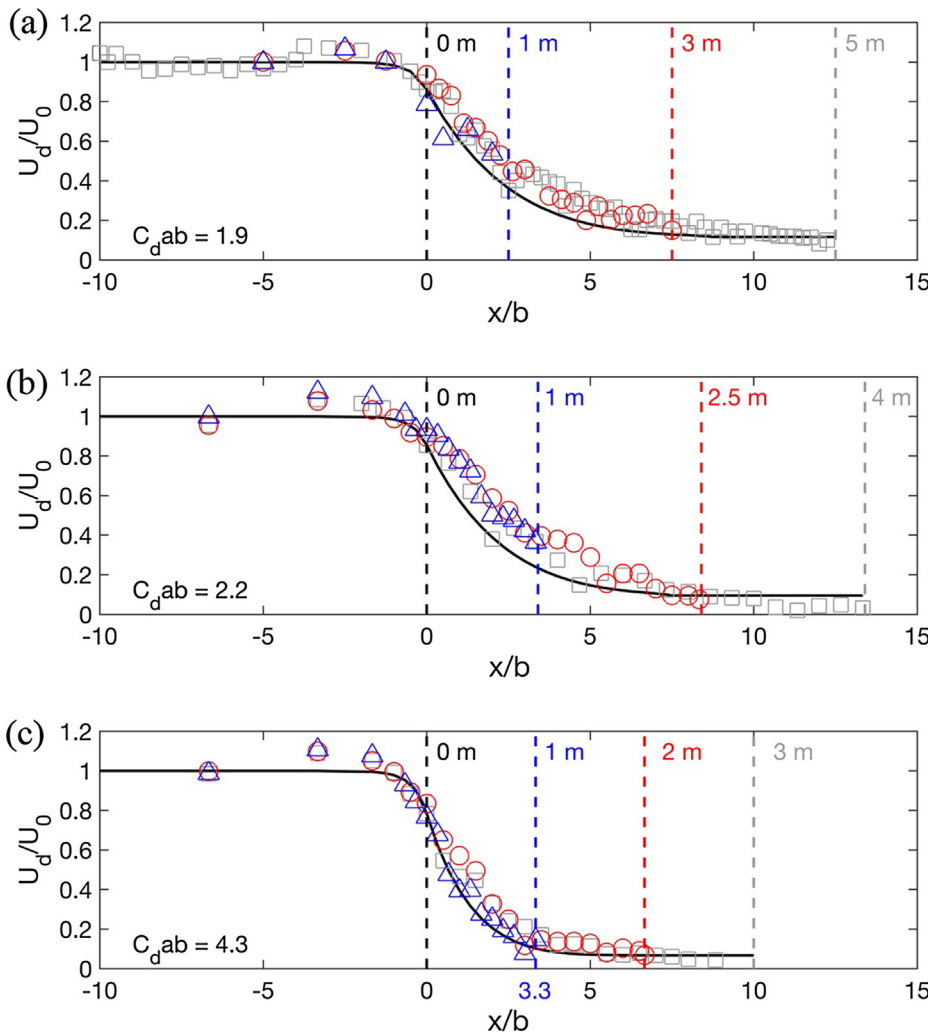


Fig. 5. Measured mean depth-averaged streamwise velocity, U_d , normalized by the mean channel velocity, U_0 , (symbols) compared to the prediction by the proposed model (black solid line), based on the data of Cases 1–9 (parameters listed in Table 1). (a) $C_{dab} = 1.9$ (Case 1–3), blue triangles, red circles and gray squares indicate velocity profiles for 1-, 3- and 5-m-long arrays, respectively. (b) $C_{dab} = 2.2$ (Case 4–6), blue triangles, red circles and gray squares indicate velocity profiles for 1-, 2.5- and 4-m-long arrays, respectively. (c) $C_{dab} = 4.3$ (Case 7–9), blue triangles, red circles and gray squares indicate velocity profiles for 1-, 2- and 3-m-long arrays, respectively. The uncertainty in U_d/U_0 is comparable to the symbol size. A part of the predicted profile (e.g., in (c), the solid line between $x/b = -10$ –3.3) for the 3-m-long array can describe the velocity evolution inside a 1-m-long array (blue triangles). (For interpretation of the references to colour in this figure legend, the reader is referred to the web version of this article.)

- (1) $U_{d(1)} = U_{d(2)}$ at $x = -L_u$;
- (2) $U_{d(2)} = U_{d(3)}$ at $x = 0$;
- (3) $\frac{\partial U_{d(2)}}{\partial x} = \frac{\partial U_{d(3)}}{\partial x}$ at $x = 0$;
- (4) $U_{d(3)} = U_{d(4)}$ at $x = L_l$.

5. Published data

The published experimental data from Rominger and Nepf (2011), Zong and Nepf (2011) and Chen et al. (2012) were used to verify the proposed model. The three studies reported the detailed measured velocities at the centerline upstream of and inside model patches over a wide range of solid volume fractions, ϕ ($=0.02$ – 0.38), and flow blockages, C_{dab} ($=1.3$ – 8.4). The details of the experiments can be found in Rominger and Nepf (2011), Zong and Nepf (2011) and Chen et al. (2012). To connect the predicted velocity profile for the tendency of fine sediment deposition inside cylinder arrays, the experimental data from Liu and Nepf (2016) were chosen because their study reported both velocities and deposition inside a model patch. A brief introduction to the experiments is provided herein for convenience. A summary of the parameters in the four studies is presented in Table 2.

First, Rominger and Nepf (2011) constructed emergent model vegetation patches with different widths (12–30 cm) using rigid wooden dowels. Three cases (denoted RN1 to RN3 in Table 2) were chosen to verify the proposed model. The dowels were fitted into PVC boards with a staggered array of holes. The solid volume fraction was varied between $\phi = 0.09$ and 0.38 . The patch half-width was varied between $b = 6$ and 15 cm, and the frontal area per patch volume was varied

between $a = 0.2$ and 0.8 cm^{-1} , corresponding to flow blockages $C_{dab} = 3$ and 8 .

Second, Zong and Nepf (2011) considered a half-width patch along the right sidewall of a flume because the flow at two patch edges was symmetric. Six cases (denoted ZN1 to ZN6 in Table 2) were used to verify the proposed model. In those cases, the mean channel velocities were different, i.e., $U_0 = 5.0, 9.0$ and 11.6 cm/s . Two frontal areas per patch volume $a = 0.04$ and 0.21 cm^{-1} were considered, leading to flow blockages $C_{dab} = 1.6$ and 8.4 , respectively. The solid volume fraction was $\phi = 0.02$ and 0.1 .

Third, Chen et al. (2012) measured the velocity profile upstream of and inside a circular model patch with $C_{dab} = 1.3$. The diameter of the patch was $D = 42 \text{ cm}$ (the half patch width was $b = 21 \text{ cm}$). The mean upstream velocity was $U_0 = 9.8 \text{ cm/s}$, and the flow depth was $h = 13.3 \text{ cm}$. The solid volume fraction was $\phi = 0.03$.

Fourth, Liu and Nepf (2016) performed deposition experiments for a capsule patch with a width of 10 cm and a length of 20 cm . The half-width of the patch was $b = 5 \text{ cm}$. The mean upstream velocity was $U_0 = 9.1 \text{ cm/s}$, and the flow depth was $h = 14 \text{ cm}$. The solid volume fraction was $\phi = 0.15$. The frontal area per volume a ($=nd$) was 0.51 cm^{-1} , yielding $C_{dab} = 8$. Microscope slides were used to collect the net deposition at four positions ($x/b = 0.5, 1.5, 2.5$ and 3.5) inside the patch. A model sediment of glass spheres with $d_{50} = 5.6 \mu\text{m}$ and a density of 2.5 g/cm^3 was mixed with water in the flume. Once the fine particles and water were mixed completely, the deposition experiment started. After 4 h, the pump was stopped, and the flume was drained. After two days, the slides with deposition were removed and placed in

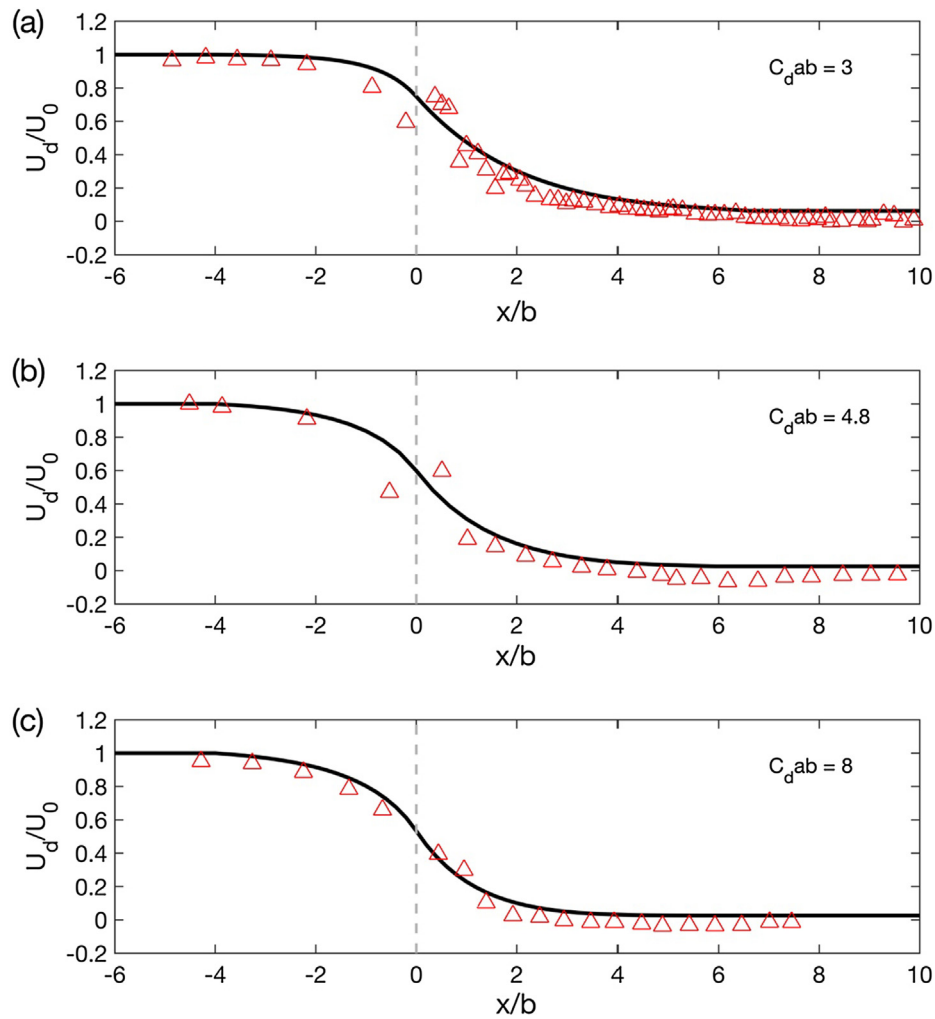


Fig. 6. Measured depth-averaged streamwise velocity, U_d , normalized by the mean channel velocity, U_0 , (triangles) compared to the prediction by the proposed model (solid lines) for patches with different flow blockages: (a) $C_d ab = 3$; (b) $C_d ab = 4.8$; and (c) $C_d ab = 8$, based on experimental data from Rominger and Nepf (2011). The mean channel velocity $U_0 = 10$ cm/s and the flow depth $h = 14$ cm are the same in the three cases. The vertical dashed line is the upstream edge of the patch ($x/b = 0$).

an oven to remove all moisture. The weight difference between the slides before and after the experiment was the net deposition. The enhanced or diminished deposition zone was determined via a comparison to the control experiment without patches (see Fig. 6 in Liu and Nepf, 2016).

Five common points among the four studies are summarized. First, all patches were emergent, and the velocities were measured at mid-depth upstream of and inside patches using a Nortek Vectrino ADV. In both regions, the differences between the velocities at mid-depth and the true depth-averaged velocities were reported to be less than 5% (White and Nepf, 2007, Liu and Nepf, 2016). It is reasonable to consider that the velocities measured at mid-depth were the same as the depth-averaged velocities. Second, the time-averaged velocity was measured at the midpoint of two cylinders and was found to differ from the true temporally and spatially averaged velocity within 20% (White and Nepf, 2007). The point velocities at the centerline are representative of temporally and spatially averaged velocities in the central region of an array for the cylinder array with $\varphi = 0.02$ – 0.1 . Third, the distance (δ) of the KH vortex penetrating the edge patch was smaller than the half patch width (b) in all cases ($\delta/b = 0.06$ – 0.39); thus, the velocities in the central region of the patch were not influenced by the vortex. Fourth, the bed friction coefficient $C_f = 0.006$ because PVC boards were used as the channel beds in all four cases. Fifth, the channel beds in the four cases were horizontal, so the free surface slope was estimated from

$S = \frac{C_f}{g h} U_0^2$. The free surface slope is summarized in Table 2 and was very small ($S < 1 \times 10^{-4}$). The influence of the change in flow depth on the streamwise velocity in the longitudinal direction was less than 1% over the experimental section. Finally, in the four studies, the cylinder Reynolds number at the upstream patch edge was $Re_{d(0)} \approx 200$ – 600 , so the drag coefficient, $C_d = 1.0 \pm 0.2$, was estimated from Eq. (3) and was used for velocity prediction.

6. Model validation

The proposed model was verified by the data in this study (Section 2) and published literature (Section 5). For all cases, because the mean channel velocity U_0 was different, the RMSEs of the depth-averaged velocity and $RMSE/U_0$ are summarized in Tables 1 and 2. First, the predicted velocities were compared to the measured depth-averaged velocity in this study. For the long patches ($L > L_b$, Cases 3, 6 and 9), the predicted and measured velocities agree well, as shown in Fig. 5 (black solid lines and gray squares, respectively). For a canopy of submerged cylinder arrays with different array lengths, Chen et al. (2013) observed that measured streamwise velocities inside such arrays collapsed onto the same line in the longitudinal direction (see Fig. 16 in their paper); thus, they suggested that the impact of the canopy length on vertical flow adjustments near the upstream patch edge is negligible. Similarly, in this study, although the lengths of the emergent arrays

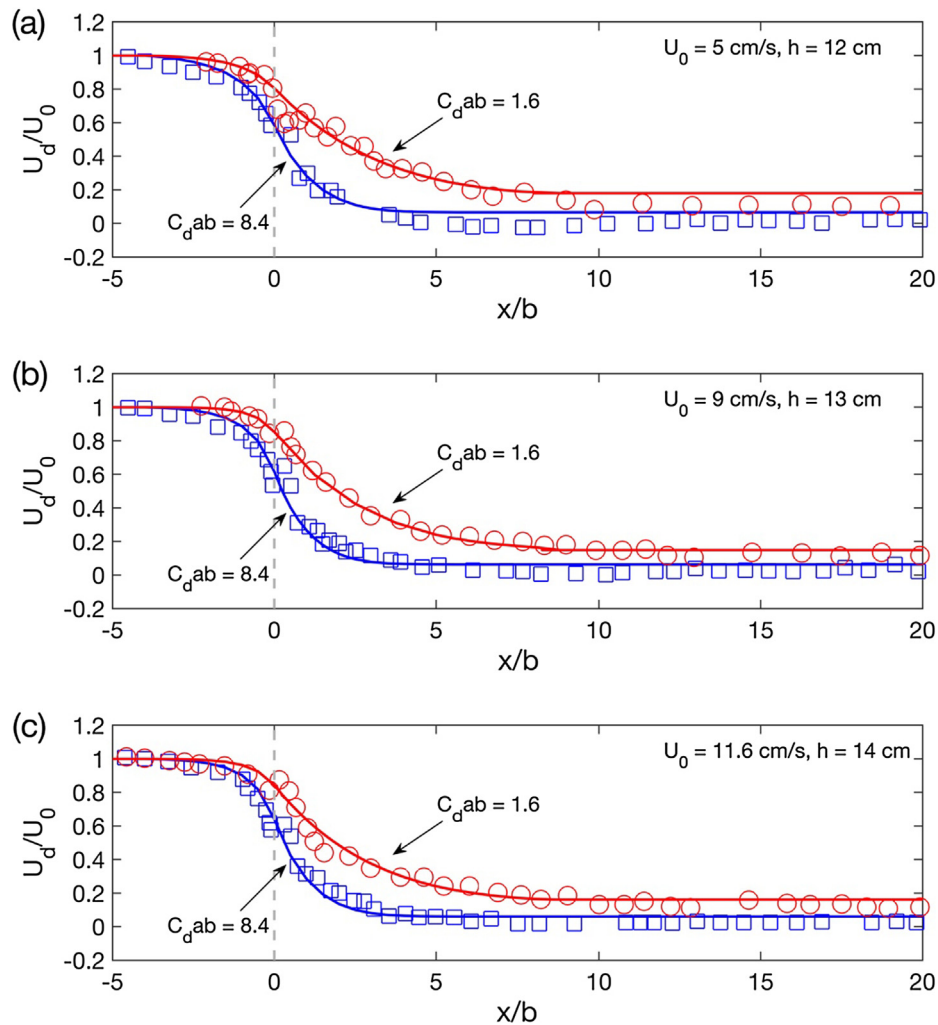


Fig. 7. Measured depth-averaged streamwise velocity, U_d , normalized by the mean channel velocity, U_0 , (circles and squares) compared to the prediction by the proposed model (solid lines) at: (a) a low-flow condition: $U_0 = 5 \text{ cm/s}$, flow depth $h = 12 \text{ cm}$; (b) a medium-flow condition: $U_0 = 9 \text{ cm/s}$, $h = 13 \text{ cm}$; and (c) a high-flow condition: $U_0 = 11.6 \text{ cm/s}$, $h = 14 \text{ cm}$. The experimental data are from Zong and Nepf (2011). The vertical dashed line is the upstream edge of the patch. Two flow blockage values ($C_{dab} = 1.6$ and 8.4) are considered under each flow condition.

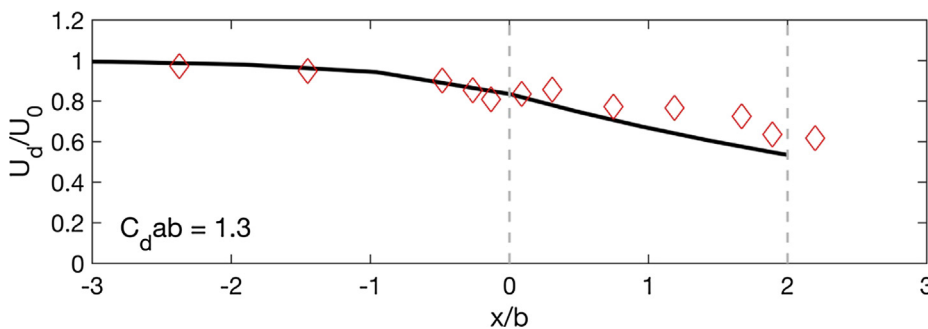


Fig. 8. Comparison between the measured depth-averaged streamwise velocity, U_d/U_0 (diamonds) and the prediction (solid line) by the proposed model at the transection along the centerline of the flume and patch, based on the data from Chen et al. (2012). The mean channel velocity $U_0 = 9.8 \text{ cm/s}$, and the flow depth $h = 13.3 \text{ cm}$. The diameter of the circular patch is $D = 2b = 42 \text{ cm}$, and the patch flow blockage is $C_{dab} = 1.3$. The two dashed lines indicate the upstream and downstream edges of the patch.

were different, the measured velocities collapsed onto the same line in the longitudinal direction (symbols in Fig. 5), indicating that the array length does not influence the lateral flow adjustment and velocity decay near the upstream edge of emergent cylinder arrays, even if the array is shorter than L_l . Based on this result, a part of the profile of the predicted velocities for the patches longer than L_l matches the measured velocities for the patches shorter than L_l . For example, in Fig. 5c, the velocity profile for the 3-m-long array was predicted (solid line), and a part of this profile ($x/b = -10$ – -3.3) matched the measured velocity for the 1-m-long patch (blue triangles). Second, the data from Rominger

and Nepf (2011) were used to verify the model. For the patches with $C_{dab} = 3, 4.8$ and 8 , the measured velocities (red triangles in Fig. 6) agree well with the prediction (solid line). Third, the data recorded in two patch densities ($C_{dab} = 1.6$ and 8.4) under three flow conditions ($U_0 = 5, 9$ and 11.6 cm/s) from Zong and Nepf (2011) were used to verify the proposed model. For patches with $C_{dab} = 1.6$ (red lines and circles in Fig. 7) and patches with $C_{dab} = 8.4$ (blue lines and squares), the model prediction agrees well with the measured velocities. Finally, the velocity data from Chen et al. (2012) were used to further verify the model predictive capability for short patches ($L < L_l$). The predicted

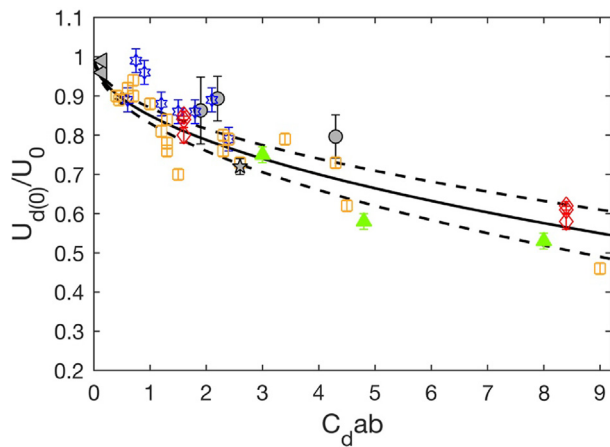


Fig. 9. Variation in the normalized depth-averaged streamwise velocity, $U_{d(0)}/U_0$, at the upstream edges of cylinder arrays with different flow blockages, C_{dab} . The data are from this study (circles), Rominger and Nepf (2011) (green triangles), Zong and Nepf (2011) (red diamonds), Chen et al. (2012) (orange squares), Liu and Nepf (2016) (pentagram), Li et al. (2018) (blue hexagrams) and Huai et al. (2015) (gray left pointing triangles). The best-fitting line (the solid line) is Eq. (17) with 95% confidence intervals (dashed lines). (For interpretation of the references to colour in this figure legend, the reader is referred to the web version of this article.)

and measured velocities agree well with each other upstream of and inside the patch (Fig. 8). Overall, for channels with vegetation patches with a wide range of flow blockages ($C_{dab} = 1.3$ – 8.4) and solid volume fractions ($\phi = 0.015$ – 0.38), the predicted depth-averaged streamwise velocities highly agree with the measured velocities. Specifically, across all cases in Tables 1 and 2, the RMSEs ranged between 0.2 and 2.5 cm/s, and the RMSEs in most cases (90%) were less than 10% of the mean channel velocity U_0 . These results indicate that the proposed model is capable of accurately predicting the longitudinal profile of velocities in the central region upstream of and inside vegetation patches.

We notice that the proposed model can present an accurate velocity profile upstream of and inside the patch (as shown in Figs. 5–8) if the velocity at the upstream patch edge, $U_{d(0)}$, is provided. However, it might not be possible to measure $U_{d(0)}$ when one applies the model. To estimate $U_{d(0)}$, a relation between the normalized velocity at the upstream patch edge, $U_{d(0)}/U_0$, and the flow blockage, C_{dab} , was built based on experimental data from this study, Rominger and Nepf (2011), Zong and Nepf (2011), Chen et al. (2012), Liu and Nepf (2016), and Li et al. (2018) and a numerical simulation by Huai et al. (2015). Li et al. (2018) considered eight groups of emergent circular model patches with $a = 0.2, 0.25, 0.3, 0.4, 0.5, 0.6, 0.7$, and 0.8 cm^{-1} and the same patch diameter, $D = 6 \text{ cm}$ (the half patch width was $b = 3 \text{ cm}$). The measured velocities at the upstream edge of the patches, $U_{d(0)}$, were extracted from Fig. 5 in Li et al. (2018). Huai et al. (2015) used a large-eddy simulation model to simulate the flow inside and outside two emergent model patches with $a = 0.01 \text{ cm}^{-1}$ and half patch width $b = 25 \text{ cm}$. In the two cases from Huai et al. (2015), the patch was the

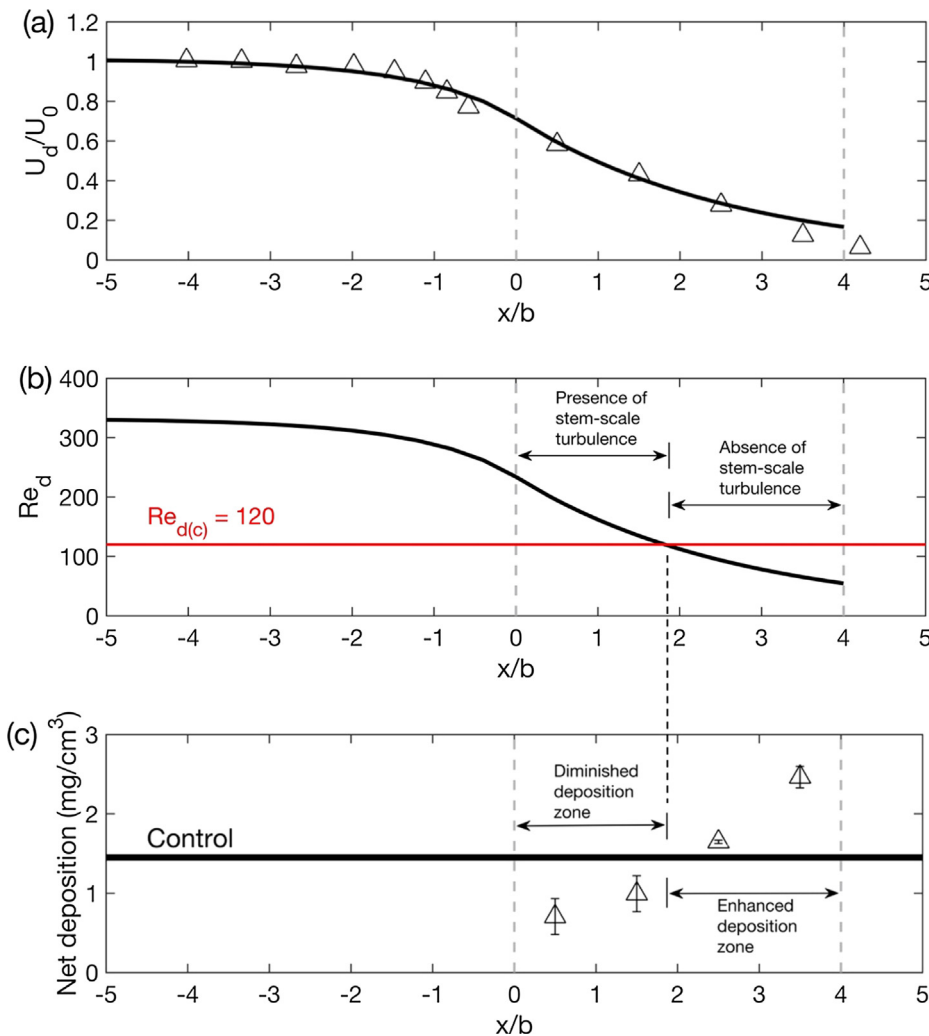


Fig. 10. Velocities, cylinder Reynolds numbers and net sediment deposition for a model patch with a width of 10 cm and length of 20 cm, based on the experimental data from Liu and Nepf (2016). The flow depth is $h = 14 \text{ cm}$, and the mean channel velocity is $U_0 = 9.1 \text{ cm/s}$. (a) The comparison between the measured depth-averaged streamwise velocities, U_d , normalized by U_0 (triangles) and the prediction of the proposed model (solid line). (b) Estimation of the region inside the model patch, over which stem-scale turbulence is present ($Re_d > Re_{d(c)}$) or absent ($Re_d < Re_{d(c)}$), based on the predicted profile of cylinder Reynolds numbers, $Re_d (= U_d d/\nu)$ (solid line), against the threshold $Re_{d(c)} (= 120, \text{ red line})$. (c) Estimated deposition region compared to the measured one, based on the net deposition inside the patch (triangles) relative to the control (black bar). The region between two dashed vertical gray lines indicates the patch ($x/b = 0$ and 4). (For interpretation of the references to colour in this figure legend, the reader is referred to the web version of this article.)

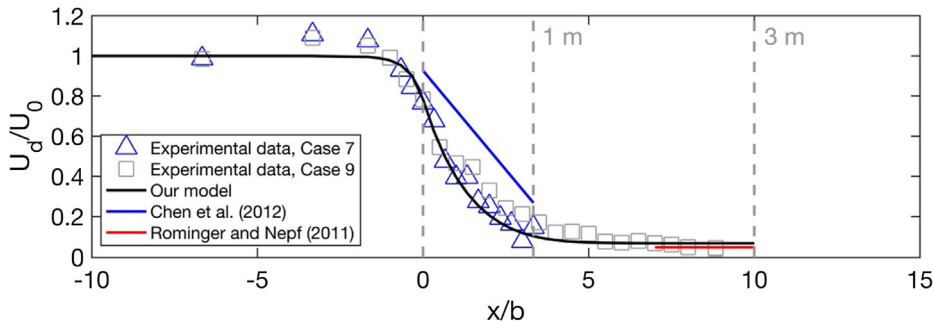


Fig. 11. Comparison between our model and those of Chen et al. (2012) and Rominger and Nepf (2011) based on the data from Cases 7 and 9 in this study. See Section 8.1 for the details of the two previous models. The Chen et al.'s model is valid for the cylinder array shorter than L_b , so their model is applied to predict the velocity profile inside a 1-m array (Case 7). Rominger and Nepf's model is only able to estimate the velocity in the fully developed flow region inside the array, so their model is used to estimate the velocity in Region 4 inside the 3-m-long array (Case 9).

same, but the flow depth was different, and the modeled $U_{d(o)}$ was extracted from Fig. 9 in their paper. Over a wide range of $C_d ab$ ($=0.4$ – 9), the measured $U_{d(o)}$ in all 19 cases extracted from Fig. 4 in Chen et al. (2012) was included. For the cases of Li et al. (2018), Huai et al. (2015) and Chen et al. (2012), the values of C_d at the leading edge of the patch were also assumed to be $C_d = 1.0 \pm 0.2$ because in all these cases, $Re_{d(o)} > 270$. For the other cases, $U_{d(o)}/U_0$ and $C_d ab$ are summarized in Tables 1 and 2. The best-fitting line (the solid line) with 95% confidence intervals (dashed lines) is shown in Fig. 9, and the equation of the best-fitting line is

$$\frac{U_{d(o)}}{U_0} = 1 - (0.15 \pm 0.02)\sqrt{C_d ab} \quad (17)$$

We note that Eq. (17) is valid only for $C_d ab = 0$ – 9 (Fig. 9). When a porous patch is sufficiently dense, $U_{d(o)}/U_0$ at the upstream edge of the patch exhibits flow patterns similar to those of a solid cylinder because very little or no flow can enter the patch; thus, the velocity at the upstream patch edge decreases to zero, i.e., $U_{d(o)}/U_0 \approx 0$. However, the critical $C_d ab$ is not reported in the published literature and is not the goal of this study. Overall, Eq. (17) can predict $U_{d(o)}/U_0$ for $9 \geq C_d ab \geq 0$, and the value of λ can then be determined using the predicted $U_{d(o)}/U_0$. When $U_{d(o)}$ is unknown, $C_d = 1$ can be initially assumed in Eq. (17). To correct $U_{d(o)}$, an iterative solution between $U_{d(o)}$ and C_d using Eqs. (3) and (17) is needed.

7. Model applications

We can use the proposed model to further estimate the deposition region of fine sediment inside a model patch. To further discuss this aspect, we take the 10-cm wide and 20-cm long capsule patch case from Liu and Nepf (2016) as an example because the velocity and sediment deposition inside the patch were reported.

First, we used the proposed model to predict the longitudinal profile of velocity; the predicted and measured velocities (solid line and triangles, respectively) are plotted in Fig. 10a. The region between the two gray dashed lines ($x/b = 0$ – 4 , with the half patch width $b = 5$ cm) indicates the patch length. The predicted profile agrees with the measured velocities with RMSE = 0.4 cm/s (corresponding to only 4% of U_0). To estimate the deposition region, the predicted longitudinal profile of velocity in Fig. 10a was then translated into the longitudinal profile of the local cylinder Reynolds number, $Re_d (= U_d d/\nu)$, in Fig. 10b. Comparing the Re_d profile (the solid line in Fig. 10b) to the threshold cylinder Reynolds number, $Re_{d(c)} (= 120)$, the red line), we can predict the region inside the patch with or without stem-scale turbulence, corresponding to $Re_d > Re_{d(c)}$ and $Re_d < Re_{d(c)}$, respectively. Thus, the diminished and enhanced deposition regions are expected to be the upstream half of the patch ($x/b = 0$ – 1.8) and the downstream half of the patch ($x/b = 1.8$ – 4), respectively. Liu and Nepf's deposition experiments confirm our estimate (Fig. 10c). However, we note that the estimation of diminished and enhanced deposition regions is based on the presence or absence of stem-scale turbulence, so this estimate is valid only for suspended fine sediment with the

ratio of settling velocity (w_s) to channel shear velocity (u_*) observed in streams, i.e., $w_s/u_* = 0.002$ – 0.3 (see the discussion in Ortiz et al., 2013). Additionally, the model cannot quantitatively predict the amount of sediment deposition.

Overall, the proposed model can accurately predict the longitudinal profile of velocities inside vegetation patches, and the predicted profile of velocity can be translated into a profile of the local cylinder Reynolds number, Re_d . Through comparison of the local Re_d and the threshold ($Re_{d(c)} = 120$), the regions with and without stem-scale turbulence can be identified, and then the diminished and enhanced deposition regions can be estimated. The proposed model could be very helpful for identifying deposition regions for fine sediment or organic matter inside vegetation patches in natural rivers or wetlands without detailed velocity measurements.

8. Discussion

8.1. Comparison to previous models

The predictive capability of the proposed model is compared to those of two previous models. First, Chen et al. (2012) proposed a model to predict the longitudinal profile of streamwise velocity at mid-depth across the centerline inside a circular array of cylinders (Eqs. (4) and (5) in their paper). In their study, the arrays were shorter than the interior adjustment length ($L < L_i$), so rapid deceleration of the flow occurred inside all arrays. Chen et al. considered the linear flow deceleration inside the arrays and presented velocity estimators for the streamwise velocities at the upstream edge of an array ($U_{d(o)}$) and the downstream edge of an array ($U_{d(e)}$):

$$\frac{U_{d(o)}}{U_0} = 1 - \frac{\alpha A}{\sqrt{\left(\frac{(1-\phi)}{C_d ab}\right)^2 + \left(\frac{1}{2}\right)^2}} \quad (18a)$$

$$\frac{U_{d(e)}}{U_0} = 1 - \frac{\beta}{\sqrt{\left(\frac{(1-\phi)}{C_d ab}\right)^2 + \left(\frac{1}{2}\right)^2}} \quad (18b)$$

where α , A and β are nondimensional parameters. Chen et al. (2012) reported $\alpha A = 0.04$ and $\beta = 0.42$ in Eqs. (18a) and (18b), respectively.

Second, for the cylinder array with $C_d ab \geq 2$, Rominger and Nepf (2011) estimated the streamwise velocity in the fully developed flow region inside the array (Region 4 in Fig. 1) as follows:

$$\frac{U_d}{U_0} = \sqrt{\frac{C_f(1-\phi)}{h C_d a}} \quad (19)$$

We chose Cases 7 and 9 of this study to perform the comparison. Case 7 has an array shorter than L_i , so the model of Chen et al. (2012) can be used to predict the deceleration of velocity inside the array. Case 9 has an array with $c_d ab (= 4.3 > 2)$ and longer than L_i , so the model of Rominger and Nepf (2011) can be used to predict the velocity in Region 4.

The predictions of the proposed model and the models of Chen et al.

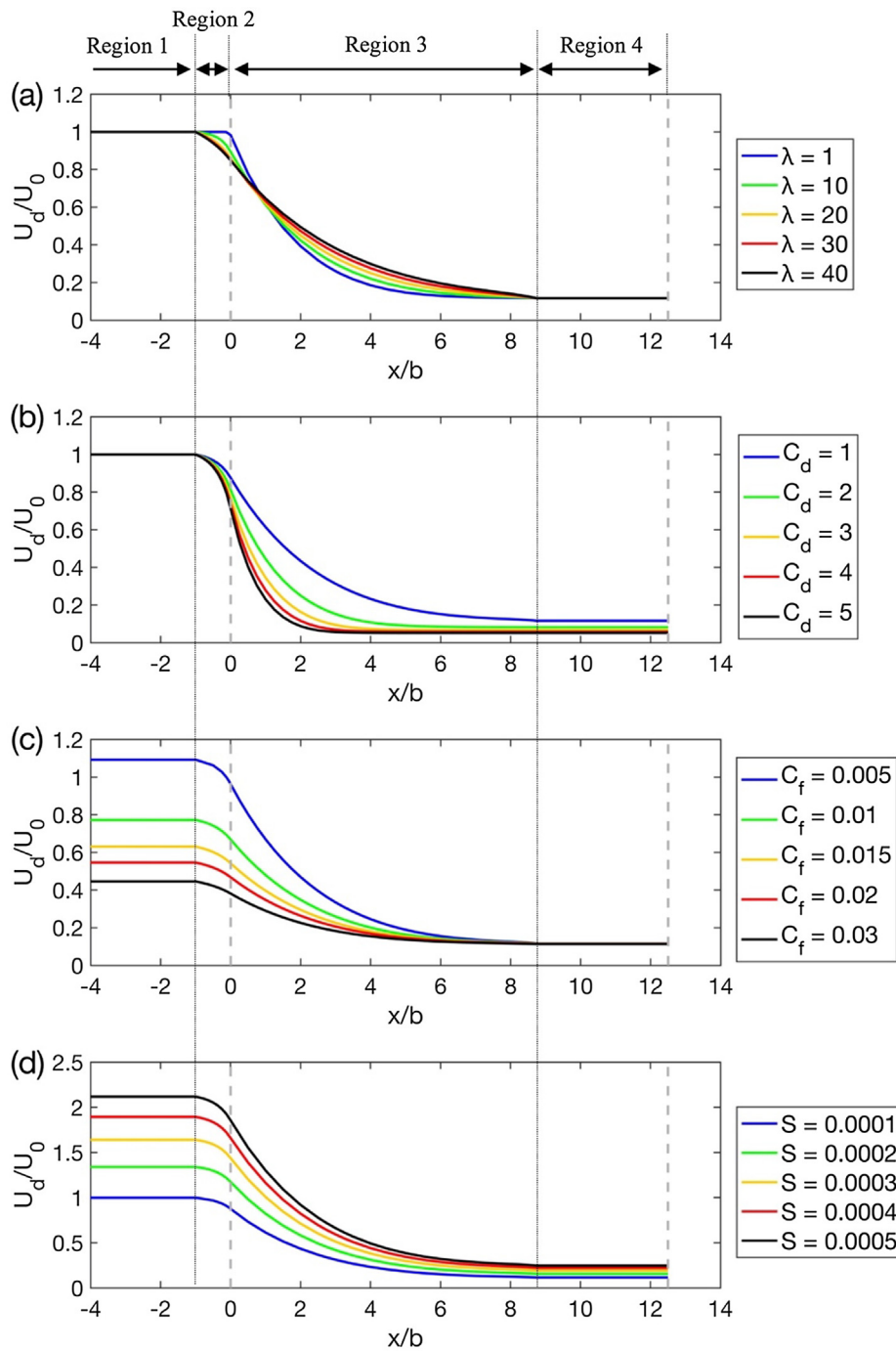


Fig. 12. Sensitivity analysis of four parameters: (a) dimensionless parameter, λ ; (b) drag coefficient, C_d ; (c) bed-friction coefficient, C_f , and (d) water surface slope, S . Case 3 ($C_d ab = 1.9$) in this study is taken as an example. When the target parameter (λ , C_d , C_f or S) was changed, the other parameters were fixed, as specified in Table 1. The regions 1–4 were marked above (a). The two vertical dashed lines indicate the upstream and downstream edges of the 5-m array.

(2012) and Rominger and Nepf (2011) are plotted against the measured velocities in Fig. 11. The proposed model captures the velocity evolution upstream of and inside the 1-m and 3-m arrays and yields accurate velocity profiles for both arrays. However, inside the 1-m array, the linear velocity profile predicted using Chen et al.'s (2012) model does not follow the measured velocity profile, yielding an average overestimate of the velocities of 120%. Rominger and Nepf's (2011) model can accurately predict the velocity in the fully developed region in the 3-m array with an RMSE = 0.01 cm/s, but their model cannot predict velocities in the other three regions.

8.2. Sensitivity analysis for λ , C_d , C_f and S

The effects of the dimensionless parameter, λ , drag coefficient, C_d , bed friction coefficient, C_f , and water surface slope, S , on the predictive velocity profile are discussed below. We used Case 3 ($C_d ab = 1.9$) as an example in this study. When the target parameter (λ , C_d , C_f or S) was changed, the other parameters were fixed as specified in Table 1. First, λ impacts the predictions only in Regions 2 and 3 ($x/b = -1$ to 8.8 , Fig. 12a). Compared to a large λ (e.g., $\lambda = 40$), a small λ (e.g., $\lambda = 1$) leads to overestimation of the velocity over $x/b = -1$ to 1 but underestimation over $x/b = 1$ to 8.8 . The appropriate λ can be determined using the velocity at the upstream edge of the array (Eq. (17)). Second,

C_d ranges between 1 and 1.1 based on the flow and vegetation conditions in natural rivers (Section 2). Values of $C_d = 1$ –5 are chosen to examine the model sensitivity. In Fig. 12b, C_d primarily influences the predicted velocities in the interior adjustment region (Region 3) inside the cylinder array. A greater C_d leads to a more rapid decrease in the predicted velocities in Region 3. Third, in typical stream conditions, the water depth may be between 50 and 100 cm and $C_f = 0.01$ for sand beds (e.g., for $d_{50} = 0.6$, Sukhodolov and Sukhodolova, 2010); thus, we consider a wider range of $C_f = 0.005$ –0.03 (Fig. 12c). C_f influences the prediction in the undisturbed region (Region 1) and the two adjustment regions (Regions 2 and 3). A larger C_f corresponds to a smaller prediction, particularly in Region 1. In contrast, C_f does not change the predicted velocity deep inside the array (Region 4) because inside an array, the bed drag (C_f) is generally smaller than the vegetation drag ($\frac{1}{2} \frac{C_d a h}{1 - \phi}$), resulting in a negligible contribution in Eq. (16). Specifically, $C_f / (\frac{1}{2} \frac{C_d a h}{1 - \phi}) = 0.004$ –0.014 in this study. Finally, S mainly affects the predictions in Regions 1, 2 and 3, in which the prediction increases as S increases. In the field, S is not easy to measure; thus, it can be estimated from $S = \frac{C_f}{g h} U_0^2$, based on the measured flow depth, bed friction coefficient and mean channel velocity far upstream from the vegetation patch.

8.3. Model limitations

This model was verified for emergent cylinder arrays with a flow blockage of $C_d a b = 1.3$ –8.4 and a solid volume fraction of $\phi = 0.015$ –0.38. For patches exceeding these ranges, further verification of the model is needed. Another limitation is that the proposed model does not address flexible plants. The spatial variability in flow may be more pronounced inside a flexible array or an array with a complicated plant morphology, in which the velocity profile may exhibit a different shape relative to the velocity profile inside a cylinder array. This is because the local maximal velocity may occur anywhere inside the flexible canopy, and the position of maximum velocity is related to the local stem frontal area (e.g., Sand-Jensen and Pedersen, 2008; Defina and Bixio, 2005; Nepf and Vivoni, 2000). Inside a flexible array, the depth-averaged velocity is no longer equal to the mid-depth velocity, which may be instead determined from the vertical profile of the velocity. When the longitudinal profile of the velocity inside a flexible canopy significantly deviates from the predicted profile, the proposed model may not be able to accurately estimate the deposition region inside the canopy.

9. Summary

Based on the flow continuity equation and momentum equation, an analytical model was proposed for predicting the longitudinal profile of the streamwise depth-averaged velocity upstream of and inside model patches of emergent vegetation. The longitudinal transect in the central region of a flume and patch was divided into four regions based on two length scales regarding lateral flow adjustments upstream of and inside the patch. Analytical solutions were presented for each region. Our experimental results suggest that the patch length is not an important factor in changing the lateral flow adjustment and velocity decay near the upstream edge of model patches, so the model should be able to predict the velocity profiles for patches longer or shorter than the interior adjustment length. Twenty groups of velocity data from our experiments and four published studies (see Sections 2 and 3) were used to verify the proposed model. The predicted longitudinal profile of velocities agrees with the measured velocities, indicating that the proposed model is able to accurately predict the velocity profile in a channel with an emergent model patch. The predicted velocities can be translated into local cylinder Reynolds numbers to identify the presence or absence of stem-scale turbulence and further estimate the diminished

or enhanced deposition of fine sediment or organic matter.

Declaration of Competing Interest

None.

Acknowledgments

We would like to acknowledge the financial support from the National Natural Science Foundation of China (Grant Nos. 51879175, 51709022 and 51539007) and the Huo Hua Ku Programme of Sichuan University (2018SCUH0020). We thank Chunhao Yan, Wei Sun, Sheng Huang and Kun Chen for collecting velocity data. We would like to thank the anonymous reviewers for their valuable comments and constructive suggestions, which significantly improved the quality of the paper.

References

- Bennett, S.J., Pirim, T., Barkdoll, B.D., 2002. Using simulated emergent vegetation to alter stream direction within a straight experimental channel. *Geomorphology* 44 (1), 115–126. [https://doi.org/10.1016/S0169-555X\(01\)00148-9](https://doi.org/10.1016/S0169-555X(01)00148-9).
- Bouma, T.J., Van Duren, L.A., Temmerman, S., Claverie, T., Blanco-Garcia, A., Ysebaert, T., Herman, P.M.J., 2007. Spatial flow and sedimentation patterns within patches of epibenthic structures: combining field, flume and modelling experiments. *Cont. Shelf Res.* 27 (8), 1020–1045. <https://doi.org/10.1016/j.csr.2005.12.019>.
- Chen, Z., Ortiz, A., Zong, L., Nepf, H., 2012. The wake structure behind a porous obstruction and its implications for deposition near a finite patch of emergent vegetation. *Water Resour. Res.* 48 (9), W09517. <https://doi.org/10.1029/2012WR012224>.
- Chen, Z., Jiang, C., Nepf, H., 2013. Flow adjustment at the leading edge of a submerged aquatic canopy. *Water Resour. Res.* 49 (9), 5537–5551. <https://doi.org/10.1002/wrcr.20403>.
- Choi, S.U., Kang, H., 2004. Reynolds stress modeling of vegetated open-channel flows. *J. Hydraul. Res.* 42 (1), 3–11. <https://doi.org/10.1080/00221686.2004.9641178>.
- Coon, W.F., Bernard, J.M., Seischab, F.K., 2000. Effects of a Cattail Wetland on Water Quality of Irondequoit Creek near Rochester, New York (No. 2000-4032). US Geological Survey.
- Cornacchia, L., Van De Koppel, J., Van Der Wal, D., Wharton, G., Puijalon, S., Bouma, T.J., 2018. Landscapes of facilitation: how self-organized patchiness of aquatic macrophytes promotes diversity in streams. *Ecology* 99 (4), 832–847. <https://doi.org/10.1002/ecy.2177>.
- Defina, A., Bixio, A.C., 2005. Mean flow and turbulence in vegetated open channel flow. *Water Resour. Res.* 41 (7). <https://doi.org/10.1029/2004WR003475>. W07006.
- Follett, E.M., Nepf, H.M., 2012. Sediment patterns near a model patch of reedy emergent vegetation. *Geomorphology* 179, 141–151. <https://doi.org/10.1016/j.geomorph.2012.08.006>.
- Grace, James B., Harrison, Janet S., 1986. The biology of Canadian weeds. 73. *Typha latifolia* L., *Typha angustifolia* L. and *Typha x glauca* Godr. *Can. J. Plant Sci.* 66, 361–379. <https://doi.org/10.4141/cjps86-051>.
- Gu, J., Shan, Y., Liu, C., Liu, X., 2019. Feedbacks of flow and bed morphology from a submerged dense vegetation patch without upstream sediment supply. *Environ. Fluid Mech.* 19 (2), 475–493. <https://doi.org/10.1007/s10652-018-9633-5>.
- Gurnell, A.M., Bertoldi, W., Corenblit, D., 2012. Changing river channels: the roles of hydrological processes, plants and pioneer fluvial landforms in humid temperate, mixed load, gravel bed rivers. *Earth Sci. Rev.* 111 (1–2), 129–141. <https://doi.org/10.1016/j.earscirev.2011.11.005>.
- Hu, Z., Lei, J., Liu, C., Nepf, H., 2018. Wake structure and sediment deposition behind models of submerged vegetation with and without flexible leaves. *Adv. Water Resour.* 118, 28–38. <https://doi.org/10.1016/j.advwatres.2018.06.001>.
- Huai, W., Xue, W., Qian, Z., 2015. Large-eddy simulation of turbulent rectangular open-channel flow with an emergent rigid vegetation patch. *Adv. Water Resour.* 80, 30–42. <https://doi.org/10.1016/j.advwatres.2015.03.006>.
- Järvelä, J., 2005. Effect of submerged flexible vegetation on flow structure and resistance. *J. Hydrol.* 307 (1), 233–241. <https://doi.org/10.1016/j.jhydrol.2004.10.013>.
- Kim, H.S., Kimura, I., Shimizu, Y., 2015. Bed morphological changes around a finite patch of vegetation. *Earth Surf. Proc. Land.* 40 (3), 375–388. <https://doi.org/10.1002/esp.3639>.
- Kim, H.S., Kimura, I., Park, M., 2018. Numerical simulation of flow and suspended sediment deposition within and around a circular patch of vegetation on a rigid bed. *Water Resour. Res.* 54 (10), 7231–7251. <https://doi.org/10.1029/2017WR021087>.
- Leonard, L.A., Luther, M.E., 1995. Flow hydrodynamics in tidal marsh canopies. *Limnol. Oceanogr.* 40 (8), 1474–1484. <https://doi.org/10.4319/lo.1995.40.8.1474>.
- Li, W., Wang, D., Jiao, J., Yang, K., 2018. Effects of vegetation patch density on flow velocity characteristics in an open channel. *J. Hydrodyn.* <https://doi.org/10.1007/s42241-018-0086-6>.
- Lightbody, A.F., Nepf, H.M., 2006. Prediction of velocity profiles and longitudinal dispersion in salt marsh vegetation. *Limnol. Oceanogr.* 51 (1), 218–228. <https://doi.org/10.4319/lo.2006.51.1.0218>.
- Liu, C., Luo, X., Liu, X., Yang, K., 2013. Modeling depth-averaged velocity and bed shear stress in compound channels with emerged and submerged vegetation. *Adv. Water*

- Resour. 60, 148–159. <https://doi.org/10.1016/j.advwatres.2013.08.002>.
- Liu, C., Nepf, H., 2016. Sediment deposition within and around a finite patch of model vegetation over a range of channel velocity. *Water Resour. Res.* 52, 600–612. <https://doi.org/10.1002/2015WR018249>.
- Liu, C., Shan, Y., Liu, X., Yang, K., Liao, H., 2016. The effect of floodplain grass on the flow characteristics of meandering compound channels. *J. Hydrol.* 542, 1–17. <https://doi.org/10.1016/j.jhydrol.2016.07.037>.
- Liu, C., Hu, Z., Lei, J., Nepf, H., 2018. Vortex structure and sediment deposition in the wake behind a finite patch of model submerged vegetation. *J. Hydraul. Eng.* 144 (2), 04017065. [https://doi.org/10.1061/\(ASCE\)HY.1943-7900.0001408](https://doi.org/10.1061/(ASCE)HY.1943-7900.0001408).
- Lopez, F., Garcia, M., 1997. *Open-Channel Flow through Simulated Vegetation: Turbulence Modeling and Sediment Transport*. Illinois Univ at Urbana Dept of Civil Engineering.
- Nepf, H.M., Vivoni, E.R., 2000. Flow structure in depth-limited, vegetated flow. *J. Geophys. Res. Oceans* 105 (C12), 28547–28557. <https://doi.org/10.1029/2000JC900145>.
- Nepf, H.M., Ghisalberti, M., White, B.L., Murphy, E., 2007. Retention time and dispersion associated with submerged aquatic canopies. *Water Resour. Res.* 43, W04422. <https://doi.org/10.1029/2006WR005362>.
- Nicolle, A., Eames, I., 2011. Numerical study of flow through and around a circular array of cylinders. *J. Fluid Mech.* 679, 1–31. <https://doi.org/10.1017/jfm.2011.77>.
- Ortiz, A.C., Ashton, A., Nepf, H., 2013. Mean and turbulent velocity fields near rigid and flexible plants and the implications for deposition. *J. Geophys. Res. Earth Surf.* 118 (4), 2585–2599. <https://doi.org/10.1002/2013JF002858>.
- Poggi, D., Porporato, A., Ridolfi, L., Albertson, J.D., Katul, G.G., 2004. The effect of vegetation density on canopy sub-layer turbulence. *Bound.-Layer Meteorol.* 111, 565–587. <https://doi.org/10.1023/B:BOUN.0000016576.05621.73>.
- Rominger, J.T., Nepf, H.M., 2011. Flow adjustment and interior flow associated with a rectangular porous obstruction. *J. Fluid Mech.* 680, 636–659. <https://doi.org/10.1017/jfm.2011.199>.
- Sand-Jensen, K., 1998. Influence of submerged macrophytes on sediment composition and near-bed flow in lowland streams. *Freshwater Biol.* 39 (4), 663–679. <https://doi.org/10.1046/j.1365-2427.1998.00316.x>.
- Sand-Jensen, K., Pedersen, M.L., 2008. Streamlining of plant patches in streams. *Freshwater Biol.* 53 (4), 714–726. <https://doi.org/10.1111/j.1365-2427.2007.01928.x>.
- Schoelynck, J., et al., 2012. Self-organised patchiness and scale-dependent bio-geomorphic feedbacks in aquatic river vegetation. *Ecography* 35 (8), 760–768. <https://doi.org/10.1111/j.1600-0587.2011.07177.x>.
- Shan, Y., Liu, X., Yang, K., Liu, C., 2017. Analytical model for stage-discharge estimation in meandering compound channels with submerged flexible vegetation. *Adv. Water Resour.* 108, 170–183. <https://doi.org/10.1016/j.advwatres.2017.07.021>.
- Shan, Y., Huang, S., Liu, C., Guo, Y., Yang, K., 2018. Prediction of the depth-averaged two-dimensional flow direction along a meander in compound channels. *J. Hydrol.* 565, 318–330. <https://doi.org/10.1016/j.jhydrol.2018.08.004>.
- Sukhodolov, A.N., Sukhodolova, T.A., 2010. Case study: effect of submerged aquatic plants on turbulence structure in a lowland river. *J. Hydraul. Eng.* 136 (7), 434–446. [https://doi.org/10.1061/\(ASCE\)HY.1943-7900.0000195](https://doi.org/10.1061/(ASCE)HY.1943-7900.0000195).
- Tal, M., Paola, C., 2010. Effects of vegetation on channel morphodynamics: results and insights from laboratory experiments. *Earth Surf. Proc. Land.* 35 (9), 1014–1028. <https://doi.org/10.1002/esp.1908>.
- van Wesenbeeck, B.K., Van De Koppel, J., Herman, P.M.J., Bouma, T., 2008. Does scale-dependent feedback explain spatial complexity in salt-marsh ecosystems? *Oikos* 117 (1), 152–159. <https://doi.org/10.1111/j.2007.0030-1299.16245.x>.
- Vandenbruwaene, W., Temmerman, S., Bouma, T.J., Klaassen, P.C., de Vries, M.B., van Callaghan, D.P., Steeg, P., van Dekker, F., Duren, L.A., Martini, E., Balke, T., Biermans, G., Schoelynck, J., Meire, P., 2011. Flow interaction with dynamic vegetation patches: implications for biogeomorphic evolution of a tidal landscape. *J. Geophys. Res.-Earth Surface* 116 (F1), 155–170. <https://doi.org/10.1029/2010JF001788>.
- Vionnet, C.A., Tassi, P.A., Martín Vide, J.P., 2004. Estimates of flow resistance and eddy viscosity coefficients for 2D modeling on vegetated floodplains. *Hydrol. Process.* 18 (15), 2907–2926. <https://doi.org/10.1002/hyp.5596>.
- White, F.M., 1991. *Viscous Fluid Flow*, second ed. McGraw-Hill, New York.
- White, B.L., Nepf, H.M., 2007. Shear instability and coherent structures in shallow flow adjacent to a porous layer. *J. Fluid Mech.* 593, 1–32. <https://doi.org/10.1017/S0022112007008415>.
- White, B.L., Nepf, H.M., 2008. A vortex-based model of velocity and shear stress in a partially vegetated shallow channel. *Water Resour. Res.* 44 (1), W01412. <https://doi.org/10.1029/2006WR005651>.
- Yang, K., Cao, S., Knight, D.W., 2007. Flow patterns in compound channels with vegetated floodplains. *J. Hydraul. Eng.* 133 (2), 148–159. [https://doi.org/10.1061/\(ASCE\)0733-9429\(2007\)133:2\(148\)](https://doi.org/10.1061/(ASCE)0733-9429(2007)133:2(148)).
- Yang, J.Q., Kerger, F., Nepf, H.M., 2015. Estimation of the bed shear stress in vegetated and bare channels with smooth beds. *Water Resour. Res.* 51 (5), 3647–3663. <https://doi.org/10.1002/2014WR016042>.
- Zhang, J., Liang, D., Fan, X., Liu, H., 2019. Detached eddy simulation of flow through a circular patch of free-surface-piercing cylinders. *Adv. Water Resour.* 123, 96–108. <https://doi.org/10.1016/j.advwatres.2018.11.008>.
- Zong, L., Nepf, H., 2011. Spatial distribution of deposition within a patch of vegetation. *Water Resour. Res.* 47, W03516. <https://doi.org/10.1029/2010WR009516>.